RESEARCH PAPER

Multi-scale study of liquid flow in micro/nanochannels: effects of surface wettability and topology

Jie Sun · Ya Ling He · Wen Quan Tao ·
John W. Rose · Hua Sheng Wang

Abstract The paper reports parametric study, using a molecular dynamics–continuum hybrid simulation method, of liquid flow in micro/nanochannels with surface nanostructures. The effects of channel height, shape of roughening element, ratio of pitch to length of roughening element and liquid–solid bonding strengths (representing surface wettability) on the velocity and temperature boundary conditions are investigated. The velocity boundary condition is found to shift from significant slip to locking due to the blocking of the surface nanostructure. The blocking appears weak for small pitch ratio and weak liquid–solid bonding. Distorted streamlines, small random eddies and appreciable density oscillations are seen in the vicinity of the wall for small pitch ratio and strong liquid–solid bonding. On the other hand, smooth streamlines and weak density oscillations are seen for large pitch ratio and weak liquid–solid bonding. Results also reveals that: relative slip length, relative Kapitza length and minus pressure gradient vary with channel height and pitch ratio in functions of power law and approximately linear, respectively; relative slip and Kapitza lengths vary with liquid–solid bonding strength as approximately decreasing power functions (except for the strongest case), whereas minus pressure gradient varies with liquid–solid bonding strength as approximately a logarithm-like function. The effect of shape of roughening element is found to be much less significant compared with the other factors studied.

Keywords Molecular dynamics simulation · Multi-scale simulation · Velocity slip · Temperature jump · Micro/nanofluidics

J. Sun (✉) · J. W. Rose · H. S. Wang (✉)
School of Engineering and Materials Science, Queen Mary
University of London, Mile End Road, London E1 4NS, UK
e-mail: j.sun@qmul.ac.uk

H. S. Wang
e-mail: h.s.wang@qmul.ac.uk

Y. L. He · W. Q. Tao
Key Laboratory of Thermal Fluid Science and Engineering
of MOE, State Key Laboratory of Multiphase Flow
in Power Engineering, Xi'an Jiaotong University,
Xi'an 710049, Shaanxi, China

1 Introduction

Non-slip boundary condition has been commonly accepted and adopted in fluid dynamics at conventional scale. However, when the dimensions shrink to be extremely small, e.g., sub-micro or nano-scales, the continuum assumption breaks down (Gad-el-Hak 1999). For liquid channel flow, the slippage has been experimentally observed at the flow boundary on a hydrophobic wall surface (Brigo et al. 2008; Byun et al. 2008). Molecular dynamics simulation (MDS) has demonstrated that slip, non-slip and locking boundary conditions (corresponding to positive, zero and negative slippages) could all exist and the degree of slippage depends on interfacial parameters such as liquid–solid bonding strength, interfacial thermal roughness, commensurability of solid and liquid densities (Thompson and Troian 1997). The non-slip boundary condition only occurs in situations where all the factors lead to zero slippage. Similar slippage also exists for temperature, which is often called the temperature jump. The thermal boundary resistance, or the Kapitza resistance, was experimentally observed between liquid helium and solids (Swartz and Pohl 1989). The acoustic mismatch model (AMM) was used to explain the phenomenon. The MDS study has shown that the liquid–solid bonding

strength, which is directly related to the wettability of the fluid to the wall surface, plays a crucial role in determining the Kapizta resistance. The Kapitza length exhibits exponential and power functions of the liquid–solid bonding strength for non-wetting and wetting liquids (Xue et al. 2003). Further studies have revealed that the liquid–solid bonding strength greatly affects density, velocity, temperature and pressure profiles (Nagayama and Cheng 2004; Voronov et al. 2006, 2007, 2008; Kim et al. 2008b).

With rapid development in micro/nanoscale machining and processing, microstructures can now be fabricated on wall surfaces for MEMS (Byun et al. 2008; Hao et al. 2009; Woolford et al. 2009). Studies on micro/nanoflows over rough surfaces have shown their importance in the design of micro-devices. Cao et al. (2006) found that the surface nanostructure has dual effect on the surface wettability and the hydrodynamic disturbance. More recent work has revealed that the atom localization inside the rectangular cavities results in reductions of velocity values and slip length and the reductions are affected by the size of the cavities (Sofos et al. 2009).

Recent investigations have demonstrated that MDS is a powerful tool for interfacial studies because of its capability of capturing the interfacial phenomena. Yet huge computational load has greatly restricted the simulation size within tens of nanometers. On the other hand, traditional CFD becomes invalid to deal with the slippages at velocity and temperature boundaries. Therefore, the hybrid simulation method, having advantages of both MDS and CFD, emerges as a feasible solution (Hu and Li 2007) and has shown promise in multi-scale and trans-scale studies in the last decade (Mohamed and Mohamad 2010). Since the pioneering work by O'Connell and Thompson (1995), the MD–continuum hybrid simulation method has been applied to solve various fluid flow and heat transfer problems (Flekkoy et al. 2000; Wagner et al. 2002; Delgado-Buscalioni and Coveney 2003; Nie et al. 2004a, b, 2006; Delgado-Buscalioni et al. 2005a, b; Liu et al. 2007; Wang and He 2007; Xu and Li 2007; Yen et al. 2007; Li and He 2009; Sun et al. 2009, 2010, 2011b). Nie et al. (2004a) verified the feasibility of using the hybrid simulation method to study the micro/nanoflows in rough channels and showed the distinctive advantage of acquiring quantities at multi-scales. Coupling schemes were proposed and developed previously by Sun et al. (2010) and the effects of relative roughening element height on the velocity and temperature boundary conditions were investigated by Sun et al. (2011b). The present study focuses on the effects of the liquid–solid bonding, surface nanostructure and channel height.

2 Simulation method

2.1 Domain decomposition

Figure 1 shows the hybrid computational model. Liquid flows in the 2D micro/nanochannels (formed by parallel

Table 1 Simulation conditions

Index	Label	$h(\sigma)$	$w(\sigma)$	p/w	β	$H(\sigma)$	$l_x \times l_y \times l_z(\sigma)$	$l_x^P \times l_y^P \times l_z^P(\sigma)$	$l_x^C \times l_z^C(\sigma)$	$n_x^C \times n_z^C$
1–5	cir/rec/tri1/tri2/tri3_β1_p2_H61	6.64	13.83	2	1	61	$331.9 \times 7.0 \times 33.3$	$55.3 \times 7.0 \times 23.1$	331.9×20.4	6×6
6–10	cir/rec/tri1/tri2/tri3_β1_p2_H122					122	$331.9 \times 7.0 \times 64.0$		331.9×51.1	6×15
11–15	cir/rec/tri1/tri2/tri3_β1_p2_H245					245	$331.9 \times 7.0 \times 125.3$		331.9×112.4	6×33
16–20	cir/rec/tri1/tri2/tri3_β1_p2_H490					490	$331.9 \times 7.0 \times 247.9$		331.9×235.0	6×69
21–25	cir/rec/tri1/tri2/tri3_β1_p1_H61			1		61	$170.8 \times 7.0 \times 33.3$	$28.5 \times 7.0 \times 23.1$	170.8×20.4	6×6
26–30	cir/rec/tri1/tri2/tri3_β1_p1.5_H61			1.5			$253.8 \times 7.0 \times 33.3$	$42.3 \times 7.0 \times 23.1$	253.8×20.4	
31–35	cir/rec/tri1/tri2/tri3_β1_p3_H61			3			$497.9 \times 7.0 \times 33.3$	$83.0 \times 7.0 \times 23.1$	497.9×20.4	
36–40	cir/rec/tri1/tri2/tri3_β0.1_p2_H61			2	0.1		$331.9 \times 7.0 \times 33.3$	$55.3 \times 7.0 \times 23.1$	331.9×20.4	
41–45	cir/rec/tri1/tri2/tri3_β10_p2_H61				10					
46–50	cir/rec/tri1/tri2/tri3_β50_p2_H61				50					

Fig. 1 Schematics of the hybrid computational model. The *dashed box* shows the simulation domain. The shapes of the roughening elements are: **a** half-circular, **b** rectangular, **c** forward triangular, **d** backward triangular and **e** isosceles triangular
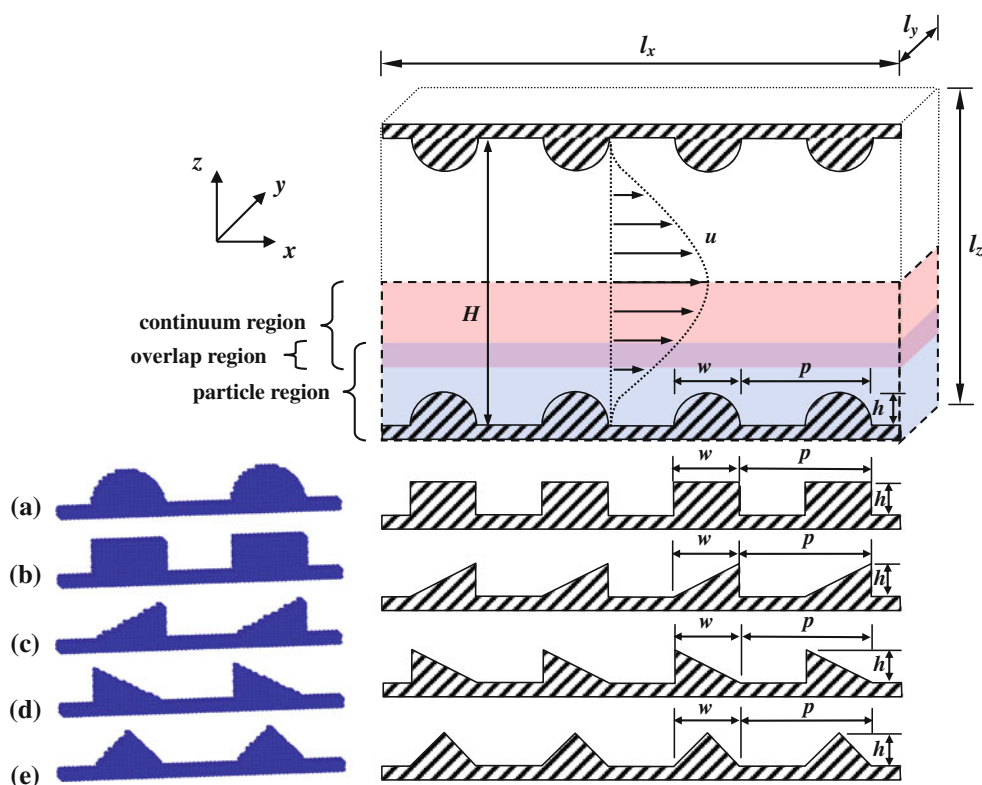
surfaces with micro/nano spacing) with five different shapes of roughening element, namely half-circular, rectangular, forward triangular, backward triangular and isosceles triangular. l_x, l_y and l_z are the overall dimensions in x-, y- and z-directions. H is the height of the channel. h, w and p are the height, length and pitch of the periodic roughening element in x-direction, respectively. Values of these quantities can be found in Table 1. Owing to symmetry, the lower half of the channel (see the dashed box in Fig. 1) is taken to be the simulation domain. The domain is decomposed into three regions, namely particle (P) region, overlap (O) region and continuum (C) region. Molecular dynamics and fluid dynamics are used to describe the mass, momentum and energy transports in P and C regions, while a set of customized coupling schemes for momentum and energy are used in O region in order to ensure the consistency between P and C regions. During each run, quantities are exchanged iteratively between P and C regions until the convergent results are obtained. The numerical methods used in each region are described below. More details are given in Sun et al. (2010, 2011b).

2.2 Molecular dynamics simulation

The classical 3D MDS serves as P solver. The settings remain the same as those used by Sun et al. (2010) and (2011b). The modified Lennard-Jones (L-J) potential

function proposed by Stoddard and Ford (1973) is used to describe the interaction between liquid molecules:

$$\varphi(r) = 4\varepsilon \left\{ \left[\left(\frac{\sigma}{r} \right)^{12} - \left(\frac{\sigma}{r} \right)^{6} \right] + \left[6 \left(\frac{\sigma}{r_c} \right)^{12} - 3 \left(\frac{\sigma}{r_c} \right)^{6} \right] \left(\frac{r}{r_c} \right)^{2} \right.$$
$$\left. - \left[7 \left(\frac{\sigma}{r_c} \right)^{12} - 4 \left(\frac{\sigma}{r_c} \right)^{6} \right] \right\} \tag{1}$$

where σ and ε are the length and energy characteristic parameters, respectively. The cut-off radius is taken to be $r_c = 2.5\sigma$. When r increases to r_c, both φ and $d\varphi/dr$ continuously go to zero, therefore no discontinuous forces will appear. Molecules outside the r_c range can be treated as free molecules. The interaction between a liquid molecule and a solid atom is also described by Eq. 1 but with different length and energy characteristic parameters of $\sigma_{ls} = 0.91\sigma$ and $\varepsilon_{ls} = \beta\varepsilon$. Here β is a factor adjusting the liquid–solid bonding strength.

The solid wall is represented by 13 layers of atoms in FCC (111) pattern at the bottom of simulation domain (see Fig. 1) with the number of atoms $N_s = 2{,}620$–$6{,}460$ and the lattice constant $\sigma_s = 0.814\sigma$. Hookean springs with the constant $k = 3{,}249.1\varepsilon\sigma^{-2}$ (Yi et al. 2002) are set between neighboring atoms. To keep the wall temperature constant at $T_w = 1.1\varepsilon k_B^{-1}$, two extra layers of "phantom atoms" are set below this configuration (Maruyama and Kimura 1999; Maruyama 2000; Sun et al. 2009). The lower layer is stationary as a frame while the upper layer is controlled with

the Langevin method, where the random force vectors to excite phantom atoms are sampled from the Gaussian distribution with mean $\mu = 0$ and standard deviation $\sigma = \sqrt{2\alpha k_B T_w / \delta t^P}$ ($\alpha = 168.3\tau^{-1}$ is the damping constant, $\delta t^P = 0.005\tau$ is the time step for P region).

The size of P region is $l_x^P \times l_y^P \times l_z^P = (28.5\sigma-83.0\sigma) \times 7.0\sigma \times 23.1\sigma$ including the thickness of the solid wall. Periodic boundary conditions are used in x- and y-directions. The upper boundary is a part of O region, which will be discussed in Sect. 2.4.

For initialization, all the space above the solid wall in P region is uniformly occupied by liquid molecules with the number of molecules $N_l = 2{,}192-9{,}216$ and the density $\rho = 0.81\ m\sigma^{-3}$ (m is the mass of a molecule). When the simulation starts, the initial period of 250τ allows the solid and liquid to reach a thermal equilibrium state at $T = 1.1\varepsilon k_B^{-1}$ (only P region operates in this period). The following period of $5{,}000\tau$ is used to let the whole system (P, C and O regions operate) to reach the steady state when the coupling between P and C regions is executed. An extra period of $2{,}500\tau$ is used to obtain the profiles of quantities by averaging. For integrating of equations of motion, the leapfrog scheme is used. For higher computational efficiency, the cell subdivision technique (Allen and Tildesley 1987; Rapaport 2004) is employed.

2.3 Finite volume method

For the 2D incompressible fluid flow, the governing equations are written as:
continuity equation:

$$\nabla \cdot \mathbf{u} = 0 \qquad (2)$$

momentum equation:

$$\frac{\partial \mathbf{u}}{\partial t} + \mathbf{u} \cdot \nabla \mathbf{u} = \frac{\mu}{\rho} \nabla^2 \mathbf{u} - \frac{1}{\rho} \nabla p \qquad (3)$$

energy equation:

$$\frac{\partial T}{\partial t} + \mathbf{u} \cdot \nabla T = \frac{\lambda}{\rho c_v} \nabla^2 T$$
$$+ \frac{\mu}{\rho c_v} \left[2\left(\frac{\partial u}{\partial x}\right)^2 + 2\left(\frac{\partial w}{\partial z}\right)^2 + \left(\frac{\partial u}{\partial z} + \frac{\partial w}{\partial x}\right)^2 \right] \qquad (4)$$

where u and w are the x- and z- components of the velocity vector $\mathbf{u}$. $\mu = 2.18\varepsilon\tau\sigma^{-3}$, $\lambda = 6.92k_B\sigma^{-1}\tau^{-1}$ and $c_v = 2.40\ k_B m^{-1}$ (NIST 2005) are the dynamic viscosity, thermal conductivity and isochoric specific heat capacity, respectively, corresponding to the liquid state of $T = 1.25\varepsilon k_B^{-1}$ and $\rho = 0.81\ m\sigma^{-3}$. The unsteady term is retained for compatibility with MDS in time evolution. Periodic

conditions are used for the inlet and outlet while a symmetric condition is used at the top boundary. The flow is assumed to be fully developed so that u, w and T are uniform along the x-direction at the bottom boundary and will be provided by P region during the simulation.

The finite volume method (FVM) is chosen and the semi-implicit method for pressure linked equations consistent (SIMPLEC) algorithm is used as C solver (Versteeg and Malalasekera 1995). The size of C region is $l_x^C \times l_z^C = (170.8\sigma-497.9\sigma) \times (20.4\sigma-235.0\sigma)$ and is uniformly divided with the mesh number of $n_x^C \times n_z^C = 6 \times 6-6 \times 69$. The simulation conditions for different cases are listed in Table 1. It should be noted that $l_x^C = n_x^C l_x^P$ is ensured to guarantee the compatibility between P and C regions in size and l_z^C / n_z^C is kept constant to save the computational time in the way of enlarging the channel by merely increasing C mesh numbers. The time step for C region is determined as $\delta t^C = 100\delta t^P = 0.5\tau$ by trial and error.

2.4 Coupling method

Liquid flow in rough channels is considered to be 2D fully developed. MDS is 3D in principle to reproduce the realistic micro-structure of the materials such as the crystalline structure. The accuracy of the information provided by P region is crucial to the performance of the hybrid solver and this can be improved by adding more molecules benefitting the extra dimension. Therefore, the O region, bridging between 3D MDS and 2D FVM, is of the key importance for the hybrid simulation method. In the present work, the O region contains three basic functional layers, i.e., the C-P, relaxation and P-C layers from the top to bottom (see Fig. 2). In C-P layer the node information is transferred to the molecules within this layer and in P-C layer the molecular dynamic information is obtained by averaging over the molecules within this layer and transferred to corresponding C nodes. Relaxation layer serves as a buffer.

In the C-P layer, the coupling schemes of momentum and energy are required for correct information transfer from the part with low degree of freedom to that with much higher degree of freedom. O'Connell and Thompson (1995) proposed a coupling scheme, primarily based on constraint dynamics, for momentum. Yen et al. (2007) improved the scheme by replacing the instant terms with time-averaging ones in order to achieve relatively higher signal-to-noise ratio and better convergent characteristics. Wang and He (2007) made a further improvement to determine the coupling parameter during computation rather than using an empirical value. Sun et al. (2010) made further modifications by introducing locally linearized constraint as well as a QUICK-type extrapolation for better

coupling performance in C-P layer. Their coupling scheme for x-momentum, as an example, is given by Eq. 5:

$$\ddot{r}_{x,i}(z,t) = f_c(t) + 2[f_4(t) - f_c(t)](z - z_c)/\Delta z^{\mathrm{C}}$$
$$+ \left[\frac{f_{x,i}(t)}{m} - \left\langle \frac{1}{N^{\mathrm{C-P}}} \sum_{j=1}^{N^{\mathrm{C-P}}} \frac{f_{x,j}(t)}{m} \right\rangle_{p\delta t^{\mathrm{P}}} \right] \quad (5)$$

where $f_c(t) = \frac{1}{(p/2+1)\delta t^{\mathrm{P}}} \left[u_c(t + \delta t^{\mathrm{P}}) - \left\langle \frac{1}{N^c} \sum_{j=1}^{N^c} \dot{r}_{x,j}(t) \right\rangle_{p\delta t^{\mathrm{P}}} \right]$

is the constraint at face c and $f_4(t) = \frac{1}{(p/2+1)\delta t^{\mathrm{P}}}$
$\left[u_4(t + \delta t^{\mathrm{P}}) - \left\langle \frac{1}{N^4} \sum_{j=1}^{N^4} \dot{r}_{x,j}(t) \right\rangle_{p\delta t^{\mathrm{P}}} \right]$ is the constraint at

node 4 (see Fig. 2). The QUICK-type extrapolation is used to obtain the quantity at face c:

$$u_c(t + \delta t^{\mathrm{P}}) = \frac{6}{8} u_3(t + \delta t^{\mathrm{P}}) + \frac{3}{8} u_4(t + \delta t^{\mathrm{P}})$$
$$- \frac{1}{8} u_2(t + \delta t^{\mathrm{P}}) \quad (6)$$

The coupling scheme for momentum in the z-direction is similar with slight geometric differences due to the staggered mesh (Versteeg and Malalasekera 1995). Based on the same concept of local linearization, Sun et al. (2010) also proposed the modified constraint equations for energy.

In P-C layer, the velocity and temperature at node 1 (see Fig. 2) are obtained by a spatial averaging within P-C layer and a temporal averaging over a period of $p\delta t^{\mathrm{P}}$ for velocity:
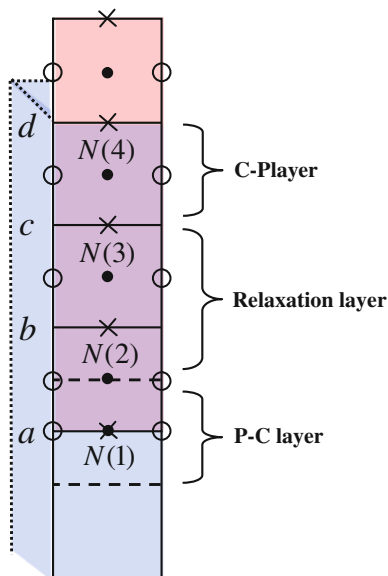
Fig. 2 Schematic of configuration in overlap region (*dot node, circle u*-velocity, *cross w*-velocity)

$$\mathbf{u}_1 = \left\langle \frac{1}{N^{\mathrm{P-C}}} \sum_{j=1}^{N^{\mathrm{P-C}}} \dot{\mathbf{r}}_j \right\rangle_{p\delta t^{\mathrm{P}}} \quad (7)$$

and for temperature:

$$T_1 = \frac{m}{3k_{\mathrm{B}}} \left\langle \frac{1}{N^{\mathrm{P-C}}} \sum_{j=1}^{N^{\mathrm{P-C}}} \left(\dot{\mathbf{r}}_j - \mathbf{u}_1 \right)^2 \right\rangle_{p\delta t^{\mathrm{P}}} \quad (8)$$

Since the flow is driven by pressure difference, the pressure gradient $-\mathrm{d}p/\mathrm{d}x$ obtained from C region should also be transferred to P region and exerted on all the molecules as an external driving force:

$$f_{\mathrm{e}} = -\frac{m}{\rho} \left(\frac{\mathrm{d}p}{\mathrm{d}x} \right) \quad (9)$$

An extra depressing force f_{d} is exerted on the molecules in C-P layer to avoid molecules drifting away (Nie et al. 2004a; Yen et al. 2007):

$$f_{\mathrm{d}}(z) = -p_0 \sigma \frac{z - z_e}{1 - (z - z_e)/\Delta z} \quad (10)$$

where p_0 is the average pressure in P region.

3 Results and discussion

Fifty cases were simulated. They are labeled as 'shape_β_p/w_H' for short, featuring different shapes of roughening element (cir: half-circular, rec: rectangular, tri1: forward triangular, tri2: backward triangular and tri3: isosceles triangular), liquid–solid bonding strengths ($\beta = 0.1, 1, 10, 50$), ratios of pitch to length of roughening element ($p/w = 1, 1.5, 2, 3$) and channel heights ($H = 61\sigma, 122\sigma, 245\sigma, 490\sigma$). Table 1 summarizes the simulation conditions. For all the cases, the maximum velocity at the center of the channel is fixed constant at $U = 1\sigma\tau^{-1}$ as the uniform standard so that the present simulation results can be compared with those in Sun et al. (2010).

### 3.1 Velocity and temperature profiles and flow and density fields

Figure 3 shows the hybrid velocity and temperature profiles as functions of z/H. Previous results for smooth channels (Sun et al. 2010) showed significant slip with the relative velocity slip (u_s/U) of about 20–2% for $H = 60\sigma$–408σ. However, in Fig. 3 the velocity boundary condition shifts from significant slip to locking because the liquid molecules are blocked by the roughening elements. The locking range and temperature jump both decrease apparently with increasing H. When the channel height is large
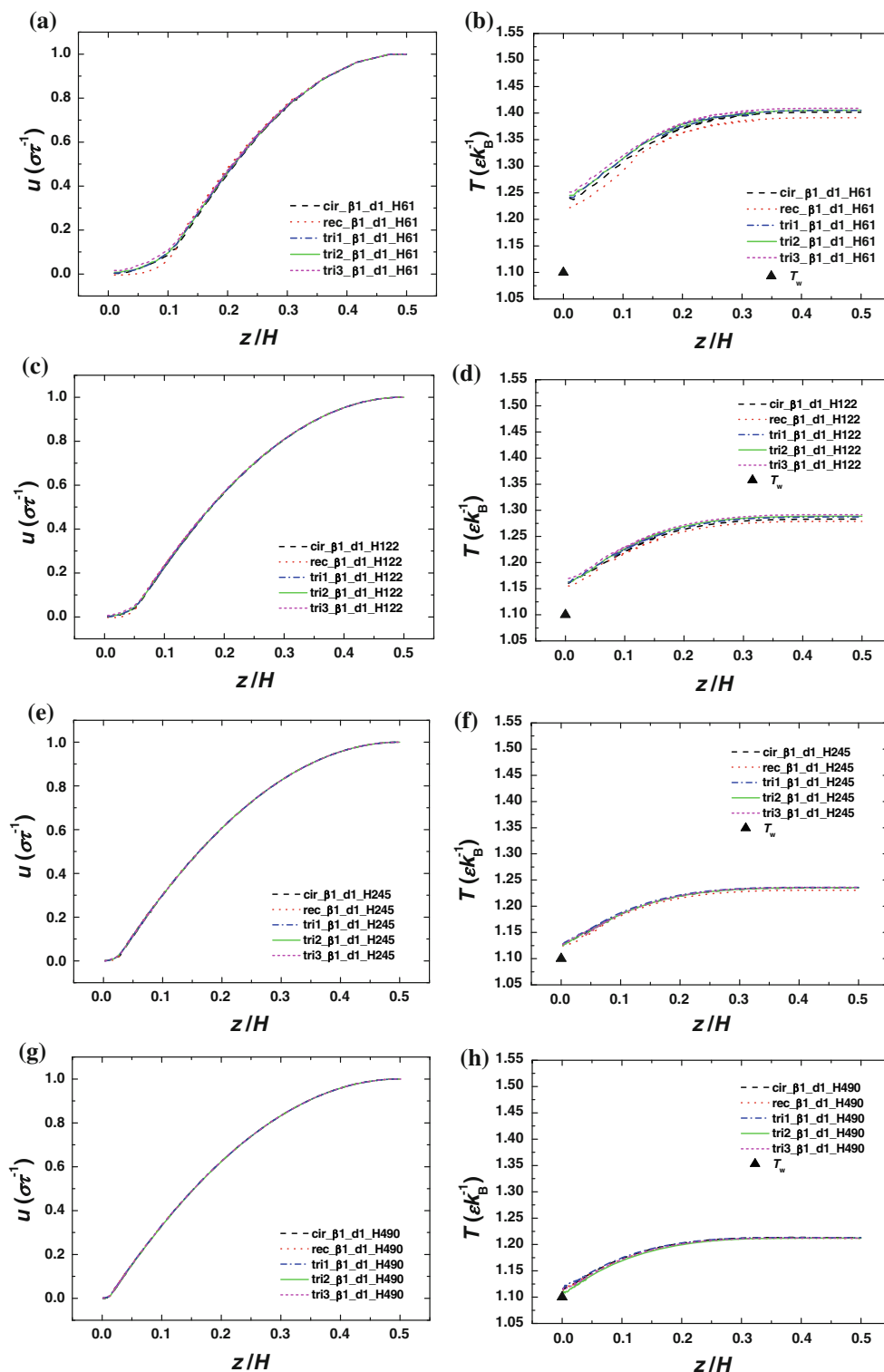
Fig. 3 Hybrid velocity and temperature profiles with different shapes of roughening element at: **a, b** $H = 61\sigma$; **c, d** $H = 122\sigma$; **e, f** $H = 245\sigma$ and **g, h** $H = 490\sigma$

enough ($H = 490\sigma$), the slippages become negligible and non-slip boundary conditions seem acceptable. As seen in the previous results (Sun et al. 2010, 2011b), all the profiles eventually converge to the analytical solution with non-slip

boundary condition when H is large enough, irrespective of the types of the boundaries at microscale (see Fig. 3a, c, e, g). Therefore, the cases with the smallest channel height ($H = 61\sigma$), where the differences can be clearly seen, were
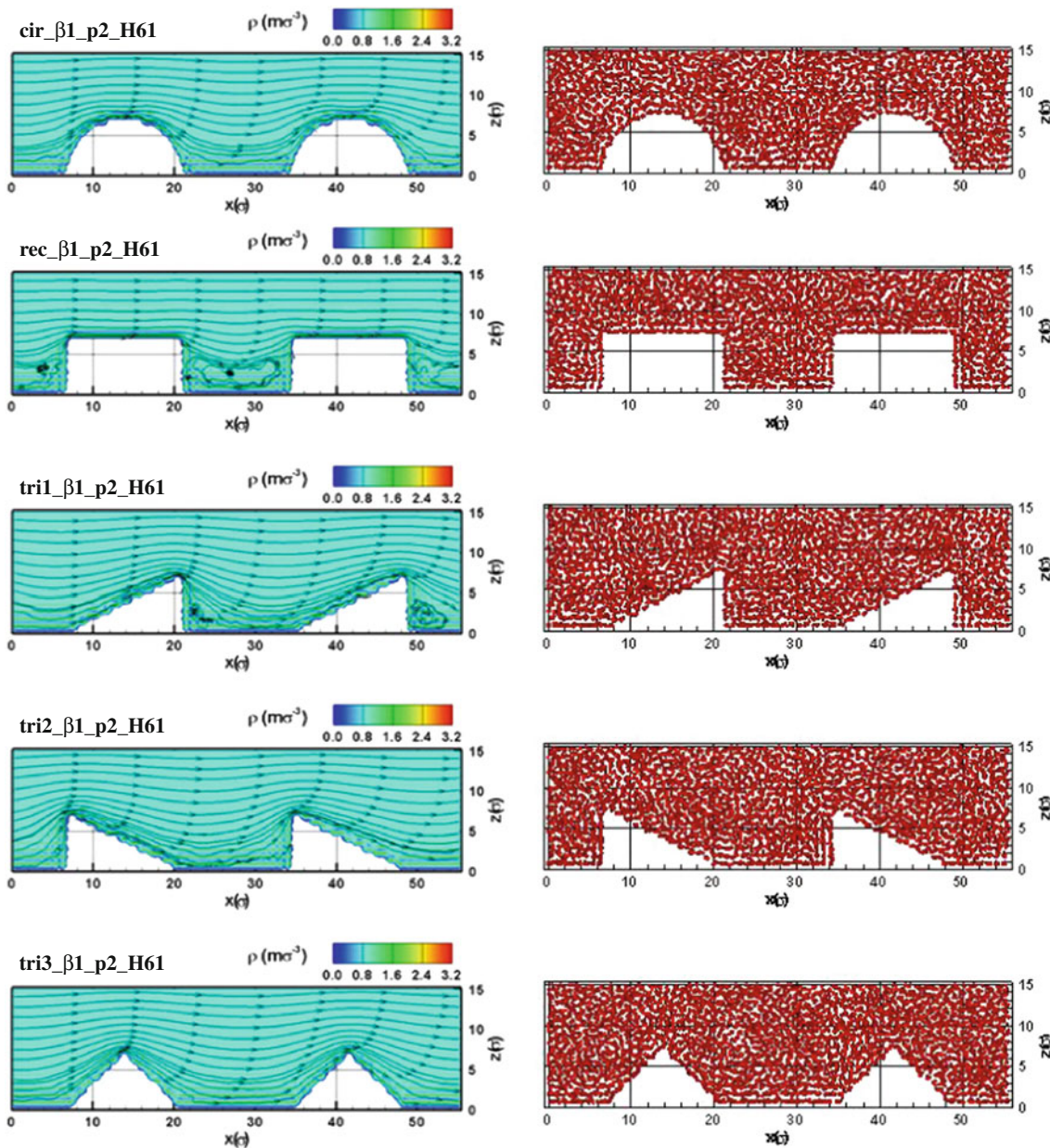
Fig. 4 Flow and density fields (*left*) and snapshots (*right*) near wall surface with different shapes of roughening element ($\beta = 1$, $p/w = 2$, $H = 61\sigma$ and snapshots are taken at $t = 7{,}750\tau$)

conducted. The rectangular case of $H = 61\sigma$ seems to have the most blocking influence, giving the thickest blocking region and smallest temperature jump.

Figures 4 and 5 show the flow and density fields and the snapshots in the vicinity of the wall for the cases of $H = 61\sigma$ and $H = 490\sigma$. The layering can be seen clearly in the density fields and the snapshots within the range of several molecular diameters from the wall surface. This interfacial layering phenomenon has been theoretically and numerically investigated in terms of liquid–solid molecular interaction (Curtin 1987; Sikkenk et al. 1987), and optically verified (Magnussen et al. 1995; Regan et al. 1995;

Huisman et al. 1997). Xue et al. (2004) found that the layering structure is the representation of liquid–solid molecular bonding strength. Stronger bonding leads to a larger range and magnitude of density oscillation. The layering structure influences the Kapitza resistance and the interfacial energy transport efficiency. The stronger bonding gives more efficient heat transfer across the liquid–solid interface. However, the layering structure itself has been proved to give no enhancement in heat transfer (Xue et al. 2004). From Figs. 4 and 5, smooth streamlines and steady vortices are seen for small channel cases while distorted streamlines and very small eddies are seen for
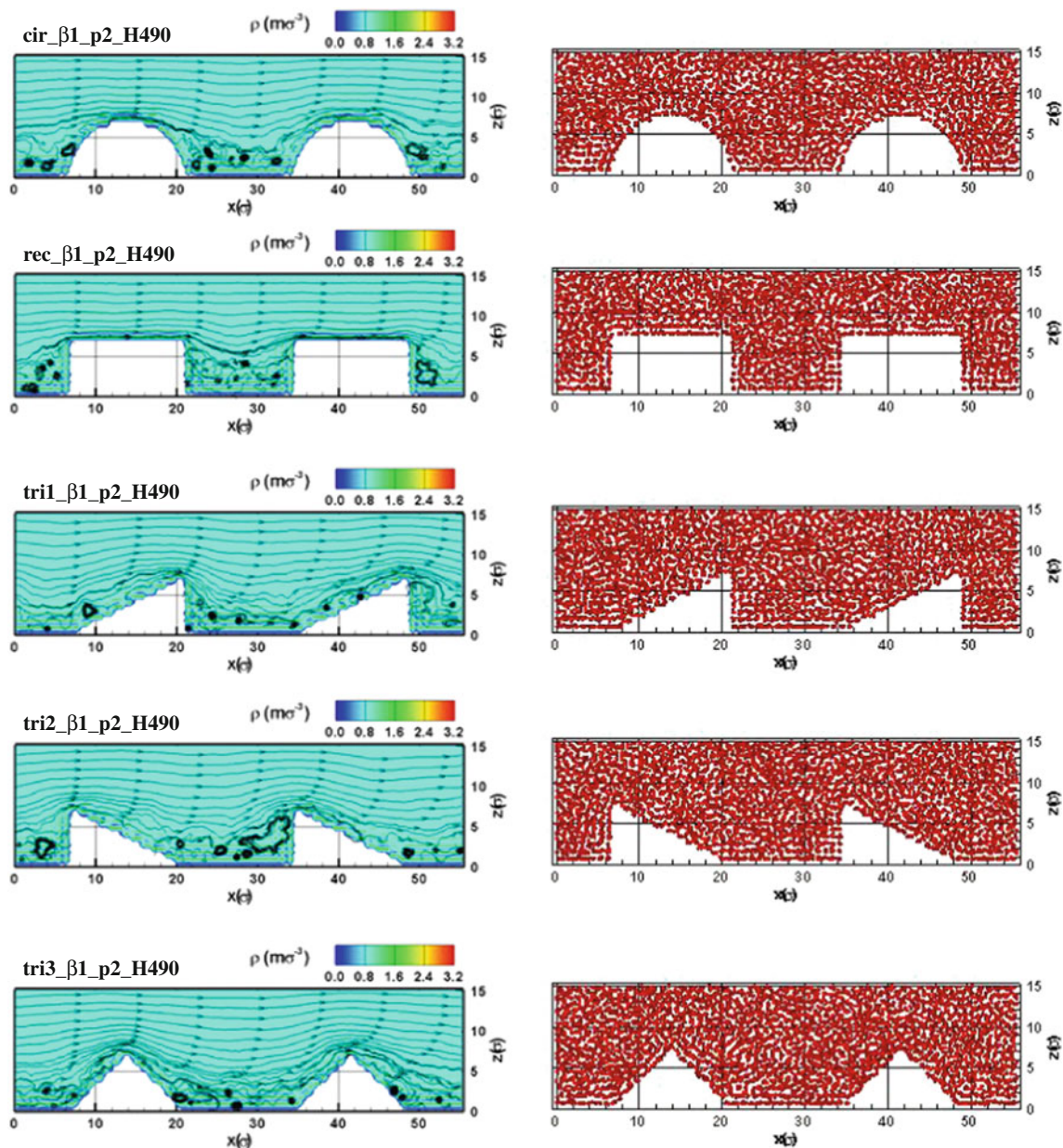
Fig. 5 Flow and density fields (*left*) and snapshots (*right*) near wall surface with different shapes of roughening element ($\beta = 1$, $p/w = 2$, $H = 490\sigma$ and snapshots are taken at $t = 7,750\tau$)

larger channel cases. From Fig. 5, the eddies exist mainly in the area covered by the density layering, especially in the corners. This suggests that the molecules forming the eddies are influenced by the balance of shear stress of the bulk flow, which tends to drive the molecules to flow away, and the liquid–solid bonding from the wall surface, which tends to lock the adjacent molecules. Since the maximum velocity is fixed, larger channel case gives smaller shear stress and the molecules are inclined to be trapped forming random eddies. The geometric blocking is noticeable because more eddies can be found in the cases with larger blocking influence (rec and tri2 cases). Moreover, more

and clearer peaks and troughs in density can be found in the concaves, especially in the corners. In the rectangular case, for example, at least five peaks and troughs can be clearly seen in the concave while only one or two on the convex is identifiable. This may be due to the fact that the molecules in the concaves are less active due to local geometric confinement, as seen in the previous study on condensation (Sun et al. 2011a).

The hybrid velocity and temperature profiles for different p/w are shown in Fig. 6. The blocking influence becomes weaker with increasing p/w. For the cases of $p/w = 1$, the velocity value within the roughening element
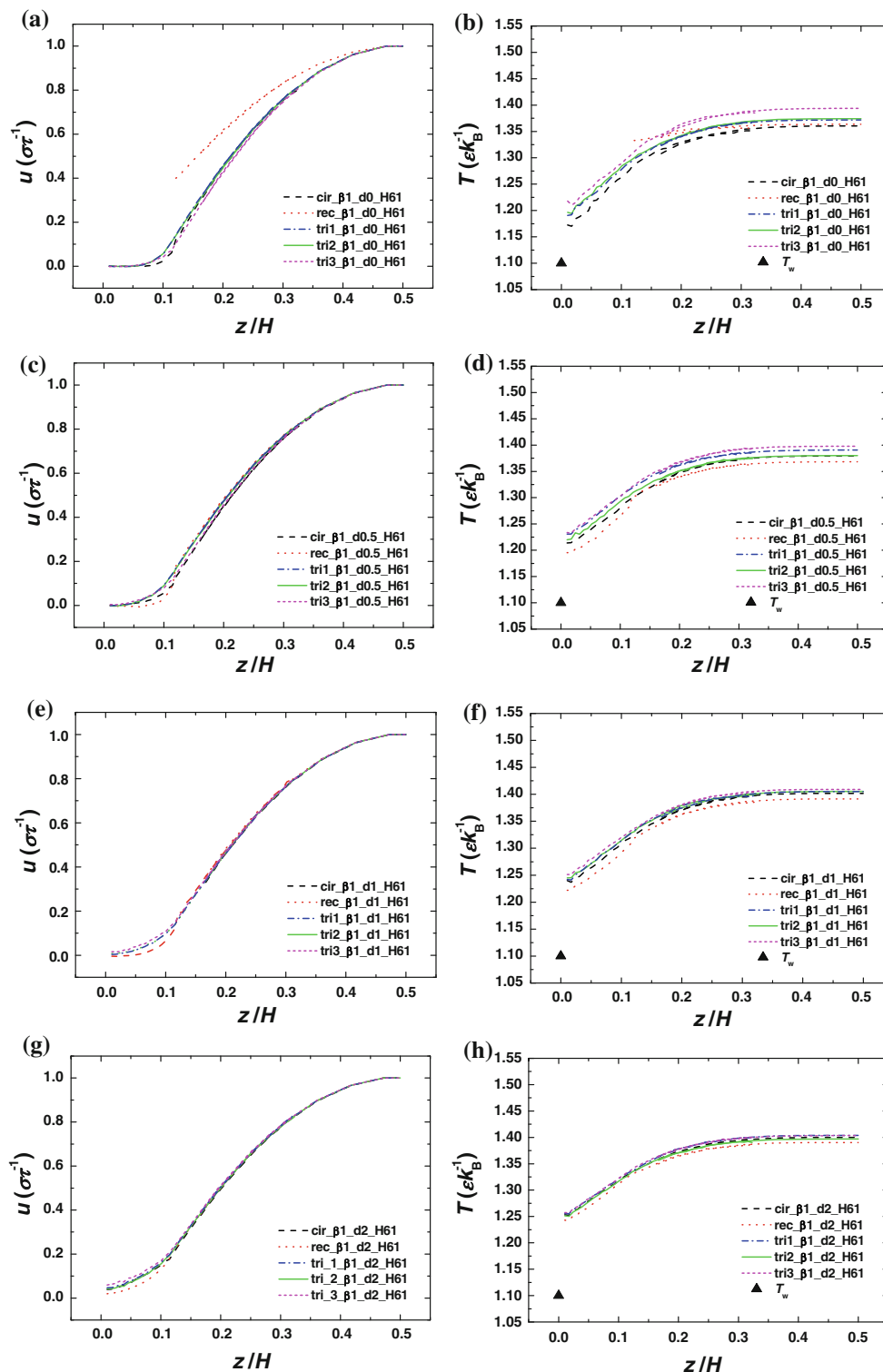
Fig. 6 Hybrid velocity and temperature profiles with different shapes of roughening element at: **a**, **b** $p/w = 1$; **c**, **d** $p/w = 1.5$; **e**, **f** $p/w = 2$ and **g**, **h** $p/w = 3$ ($H = 61\sigma$)

height is restrained at zero, while the blocking influence is so weak for the cases of $p/w = 3$ that even small slips are noticeable. It should be noted that the rectangular case always shows the most apparent confinement except the case of $p/w = 1$, where the surface becomes smooth. The geometric variation also slightly influences the temperature boundary condition. The temperature jump starts from around $0.1\varepsilon k_B^{-1}$ and then gradually increases to roughly

Fig. 7 Flow and density fields (*left*) and snapshots (*right*) near wall surface with different shapes of roughening element ($\beta = 1$, $p/w = 1$, $H = 61\sigma$ and snapshots are taken at $t = 7{,}750\tau$)
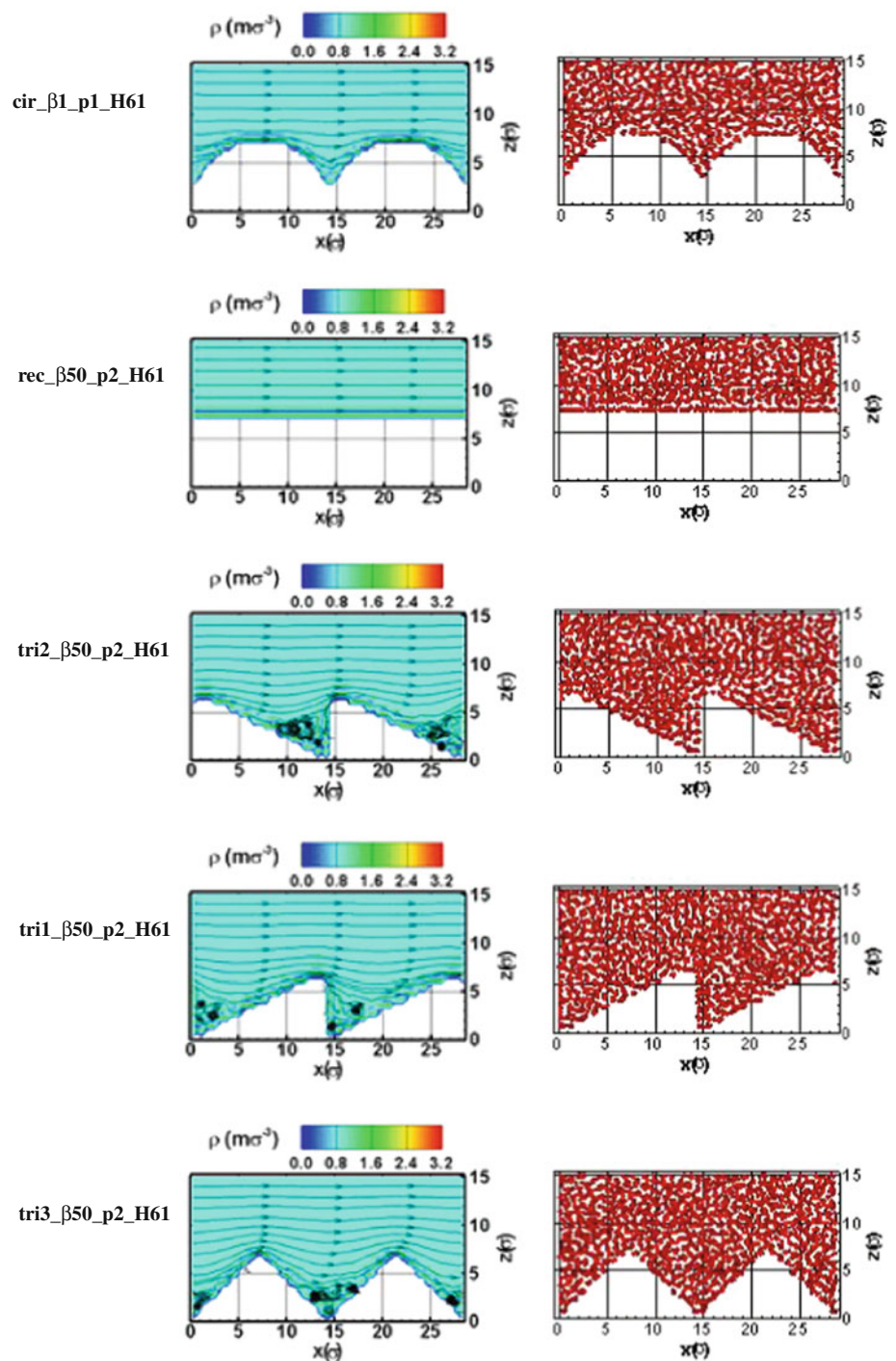
0.15$\varepsilon k_{\mathrm{B}}^{-1}$ with increasing p/w. However, the maximum temperature does not change much. More details can be found by comparing Fig. 7 with Fig. 8 that the eddies emerge in the concaves when $p/w = 1$ and totally disappear when $p/w = 3$. This indicates that the geometric confinement of the roughening elements is dependent more on p/w than the shape.

It is apparent from Fig. 9 that the variation of β has significant influence on the velocity and temperature

boundary conditions. The liquid–solid bonding strength determines the efficiency of the interfacial energy transport. Larger β means more efficient heat transfer, which causes the whole temperature profile to drop. This variation becomes more obvious for smooth cases from considerable velocity slip for small β to multi-layer locking for large β. It should be noted that when $\beta = 10$ the boundary temperatures for smooth and rough cases are almost identical and very close to T_{w} while when $\beta = 50$, this temperature
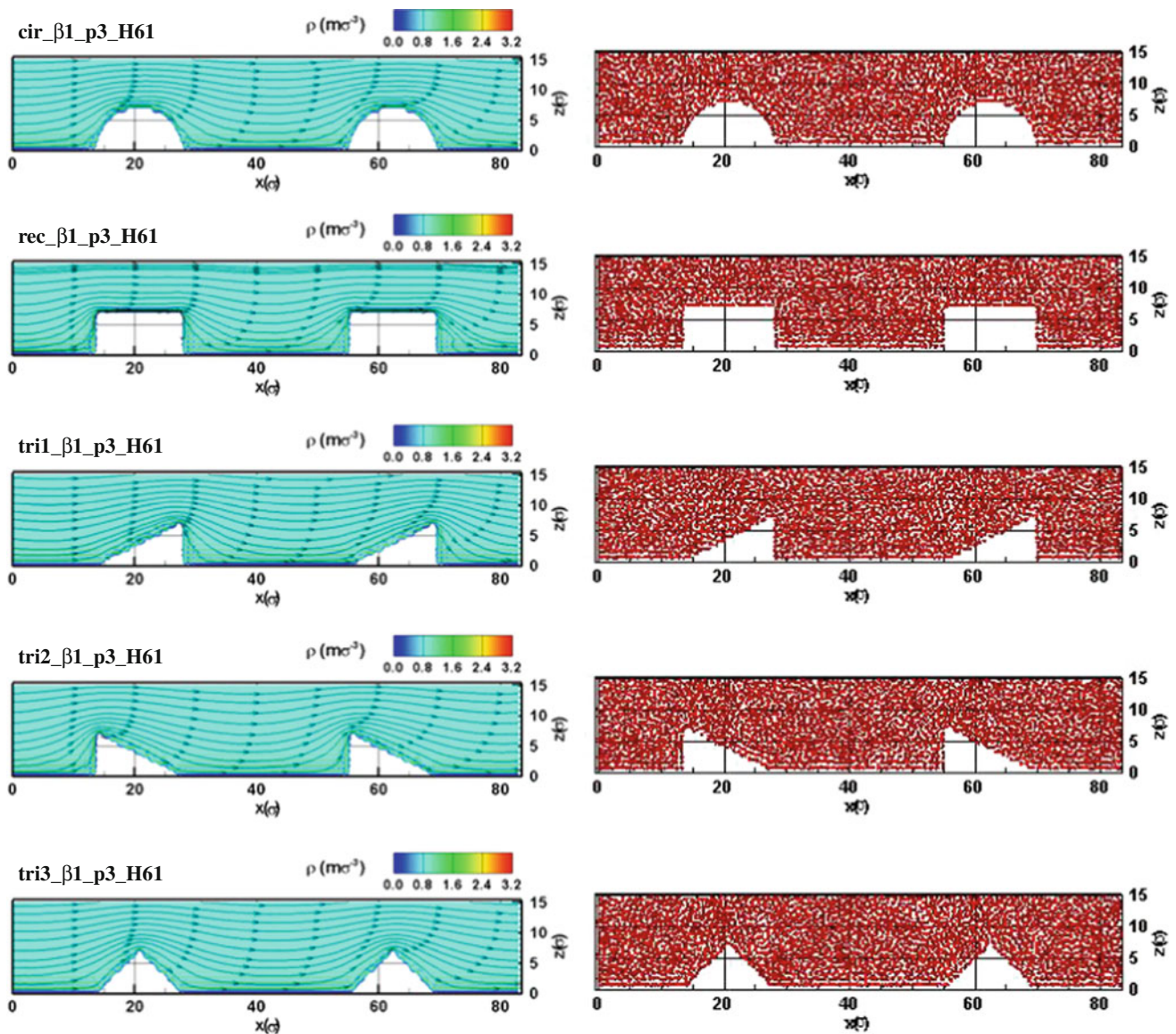
Fig. 8 Flow and density fields (*left*) and snapshots (*right*) near wall surface with different shapes of roughening element ($\beta = 1$, $p/w = 3$, $H = 61\sigma$ and snapshots are taken at $t = 7,750\tau$)

for rough cases drops even a bit lower than T_w with severe local oscillation. It is probably due to the fact that the molecules are confined so firmly that even their vibrational motions are restricted to some extent. This is supported by Figs. 10 and 11, where it is clearly shown that weak confinement on the molecules adjacent to the wall ($\beta = 0.1$) gives smooth streamlines over surface without any eddies while strong confinement ($\beta = 50$) causes significant peaks and troughs in density contour and apparent layering in the snapshots, and many small eddies and distorted streamlines in flow field. It should be mentioned that the locally linear temperature gradient observed in previous work (Sun et al. 2011b) is also found in Fig. 9f, h but is not apparent in

other cases. The reason for this is probably that larger β gives an equivalent strong confinement as the compact arrangement of the square roughening elements did in previous work (Sun et al. 2011b). In principle, a linear gradient should exist when liquid molecules are tightly restricted due to either interactive condition or geometric condition or both because only pure thermal conduction is then permitted.

3.2 Slip length and Kapitza length

The slip length (L_s) is widely used to quantitatively measure the velocity slip and is defined (Gad-el-Hak 1999) as:
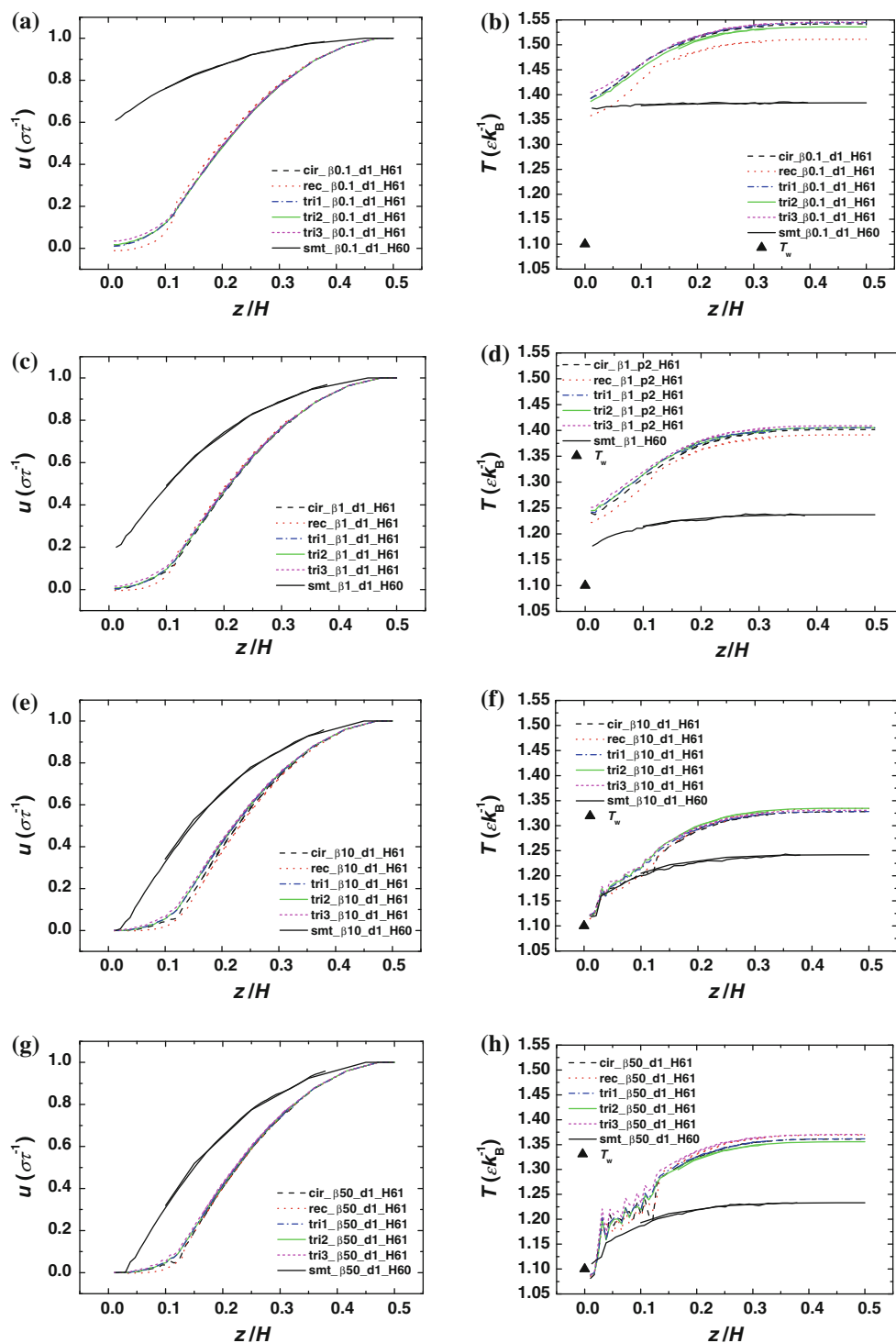
Fig. 9 Hybrid velocity and temperature profiles with different shapes of roughening element at: **a**, **b** $\beta = 0.1$; **c**, **d** $\beta = 1$; **e**, **f** $\beta = 10$ and **g**, **h** $\beta = 50$ ($H = 61\sigma$). Data for the smooth (*smt*) cases are from Sun et al. (2010)

$$L_s = u_s \left/ \frac{\partial u}{\partial n}\right|_w \tag{11}$$

where u_s is the velocity slip. Figure 12 shows the schematic for slip, non-slip and locking velocity boundary conditions

by curves a, b and c. Based on the definition by Eq. 11, the values of slip length are positive ($L_{s,a}$), zero and negative ($L_{s,c}$), respectively. Similarly, the Kapitza length (L_K) is used to measure the degree of temperature jump quantitatively and is defined (Kim et al. 2008a) as:
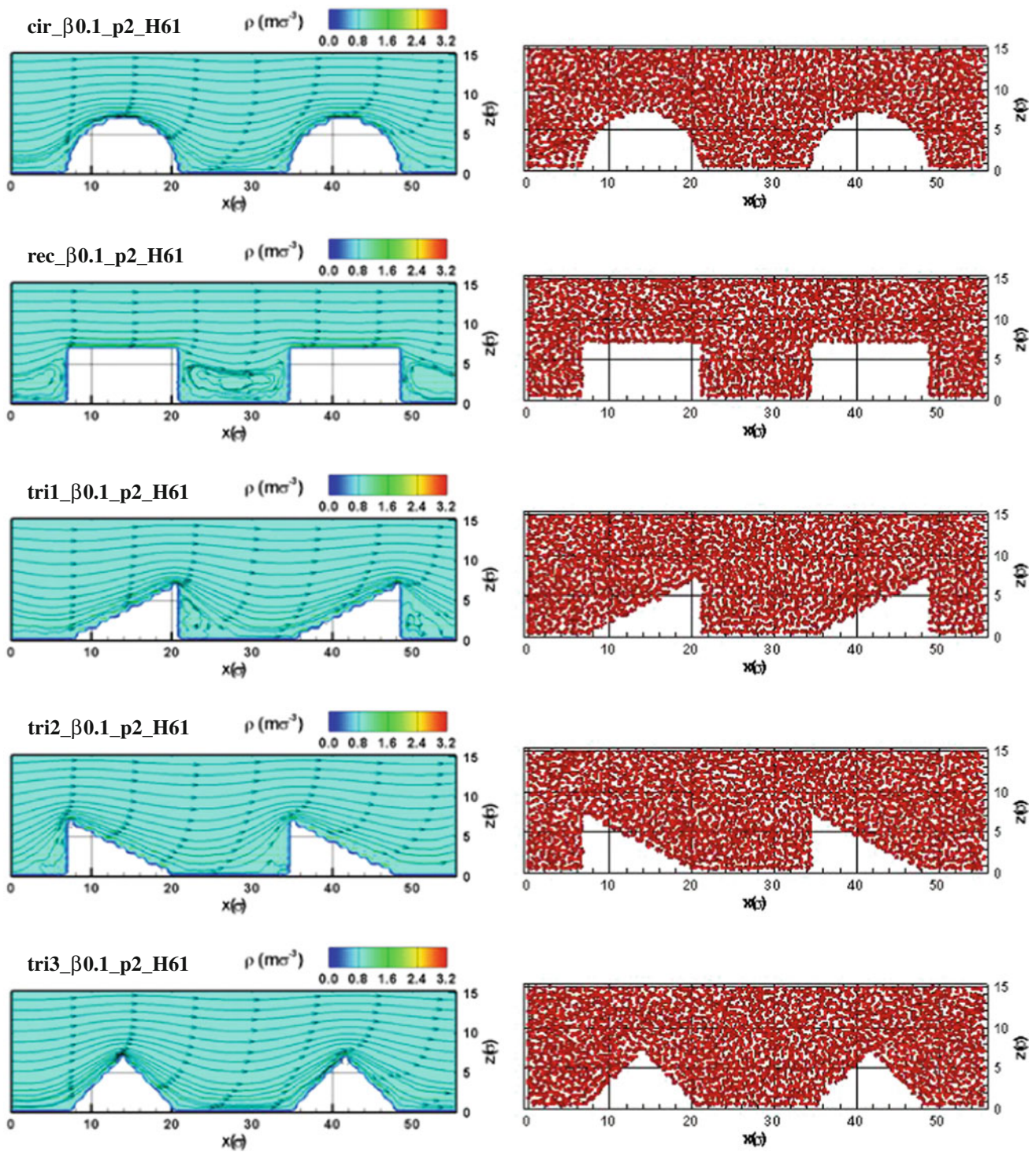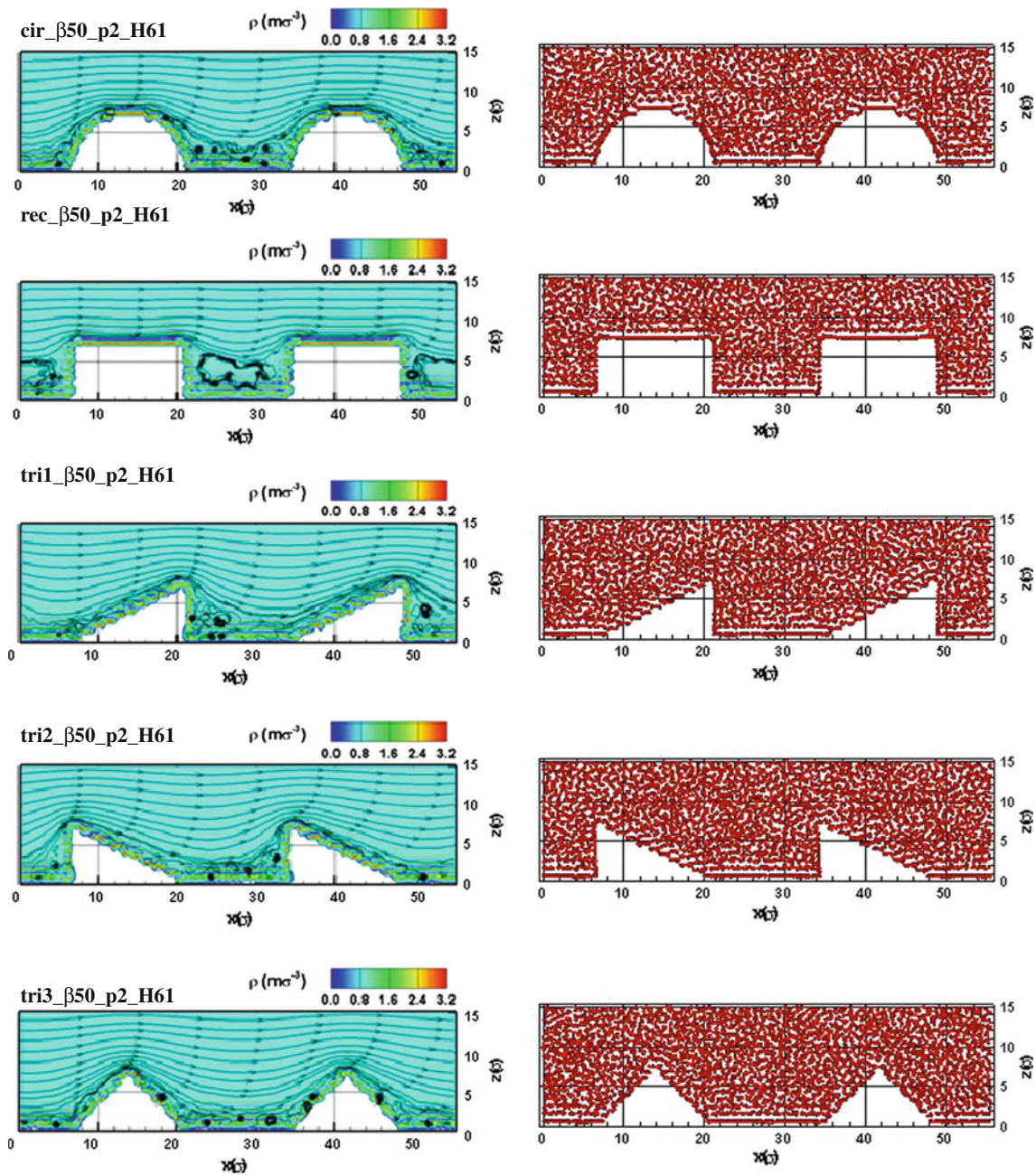
Fig. 10 Flow and density fields (*left*) and snapshots (*right*) near wall surface with different shapes of roughening element ($\beta = 0.1$, $p/w = 2$, $H = 61\sigma$ and snapshots are taken at $t = 7,750\tau$)

$$L_{\mathrm{K}} = T_{\mathrm{j}} \left/ \frac{\partial T}{\partial n}\right|_{\mathrm{w}} \qquad (12)$$

where T_{j} is the temperature jump.

The variations of relative slip length (L_{s}/H) and relative Kapitza length (L_{K}/H) versus H, p/w and β are shown in

Figs. 13 and 14. In all the cases, different shapes of roughening element give very similar variation. L_{s}/H increases sharply for small H and slightly for large H. L_{s}/H generally increases linearly with increasing p/w. L_{s}/H decreases sharply for small β and slightly for large β. L_{K}/H decreases sharply for small H and slightly for large

Fig. 11 Flow and density fields (*left*) and snapshots (*right*) near wall surface with different shapes of roughening element ($\beta = 50$, $p/w = 2$, $H = 61\sigma$ and snapshots are taken at $t = 7{,}750\tau$)

H. L_K/H generally increases with increasing p/w but the rate decreases. L_K/H decreases sharply for small β and slightly for large β. By curve-fitting, it is found that both L_s/H and L_K/H versus H still follow the power law (Sun et al. 2010; Sun et al. 2011b):

$$\frac{L_s}{H} \text{ or } \frac{L_K}{H} = a\left(\frac{H}{\sigma}\right)^b \tag{13}$$

The variations of L_s/H versus β seem similar for both smooth and rough cases. They decrease rapidly when $\beta < 5$ and then decrease slightly when $\beta > 5$. The differences are small, 0.31 to -0.029 for smooth channel cases and -0.068 to -0.11 for rough channel cases. This suggests that negative slip likely occurs in rough channels while positive, zero and negative velocity slips occur in smooth channels based on different liquid–solid
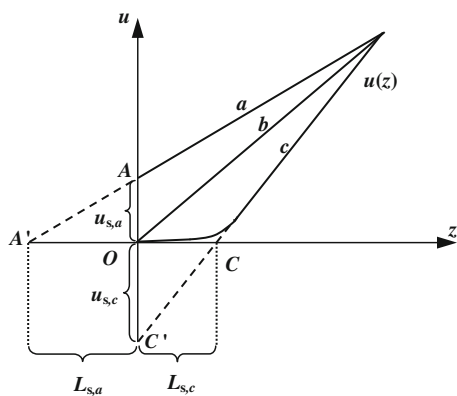
Fig. 12 Schematic of slip, non-slip and locking velocity boundary conditions

bonding strengths. L_K/H decreases rapidly with increasing β when $\beta < 10$ for both smooth and rough channels. However, the difference emerges when $\beta > 10$, where L_K/H for rough cases starts to increase (see Fig. 14c). Similar phenomenon has been found for T_j of smooth cases in the previous work (Sun et al. 2010). This characteristic is apparently related to very strong liquid–solid bonding but further studies are still needed for the insight into the mechanism and regulation. Besides, it is worth mentioning that the apparent values of u_s and T_j to calculate L_s and L_K are obtained based on fitting curves despite the local characteristics near boundaries like curve c in Fig. 12.

3.3 Flow resistance

Figure 15 shows the minus pressure gradients ($-dp/dx$) against H, p/w and β for all cases simulated. As in the smooth channel case (see Sun et al. (2010)), $-dp/dx$ versus H, irrespective of the shape of roughening element, can be well fitted by the power function:

$$-\frac{\sigma^4 dp}{\varepsilon dx} = a\left(\frac{H}{\sigma}\right)^b \qquad (14)$$

where a and b are constants determined by curve-fitting as $a = 84.84$ and $b = -2.289$. This indicates that the shape of roughening element almost shows no influence on the variation of $-dp/dx$ versus H in the present simulation range. It can be seen from Fig. 15a that the effect of surface topology on $-dp/dx$ is negligible when H is great than about 150σ whereas $-dp/dx$ for rough channels are significantly higher than those for smooth channels when H is less than about 150σ. $-dp/dx$ generally decreases linearly with increasing p/w and increases sharply for small β and slightly for large β. The value of $-dp/dx$ at $\beta = 50$ for the rectangular case is relatively low. This may be due to the very strong liquid–
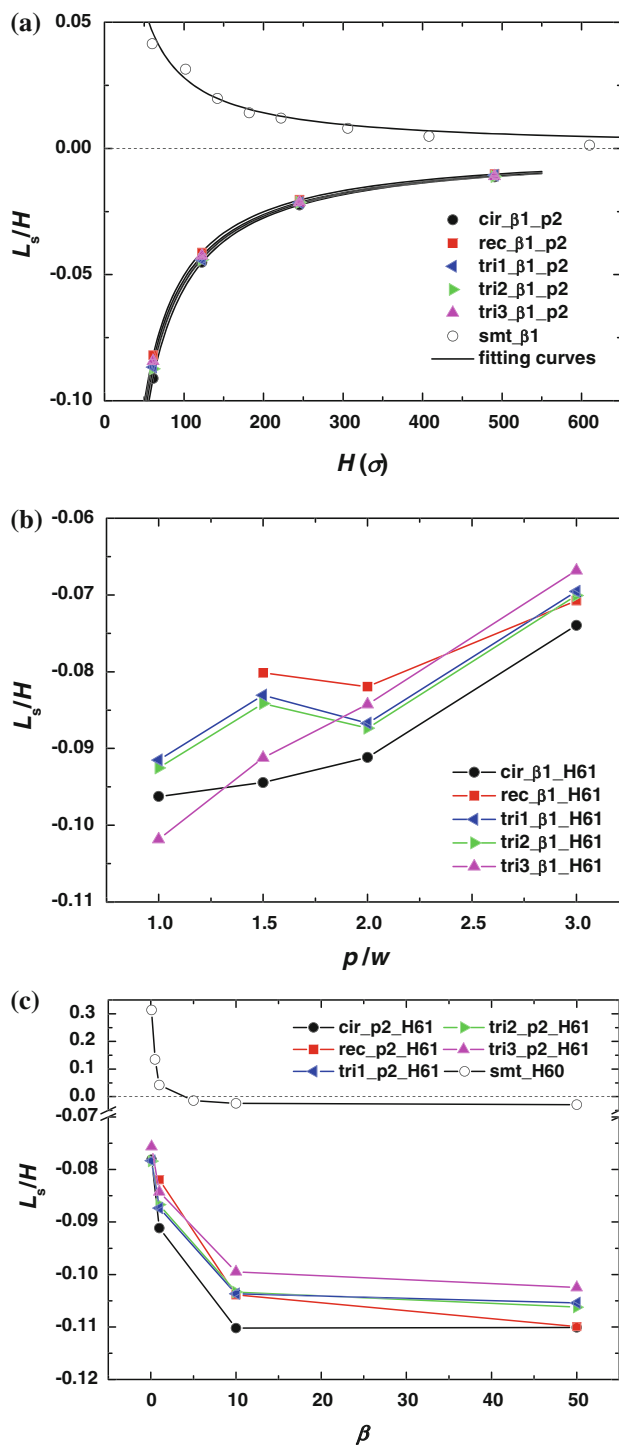
Fig. 13 Variation of relative slip length (L_s/H) versus **a** channel height (H), **b** pitch ratio (p/w) and **c** liquid–solid bonding factor (β) with different shapes of roughening element. Data for the smooth (*smt*) cases are from Sun et al. (2010). The *solid line* is a guide for the eye
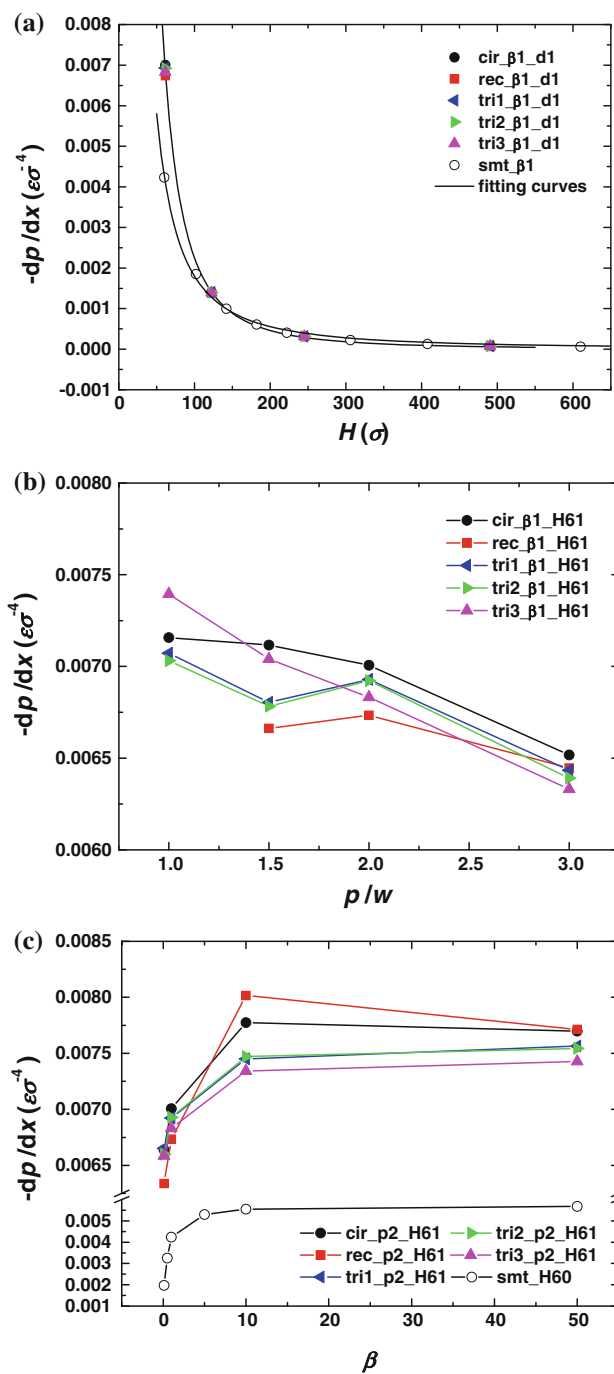
solid bonding and relatively larger contact surface area. Further investigation into the interfacial mechanism is needed.
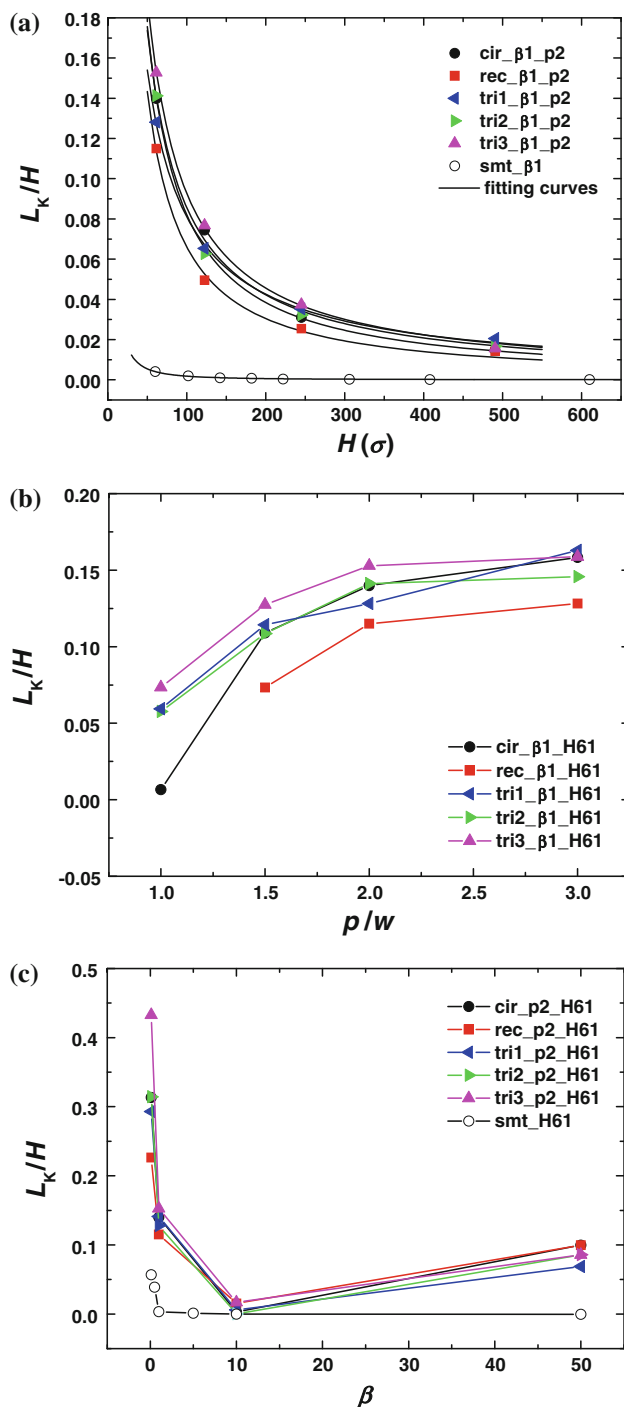
Fig. 14 Variation of relative Kapitza length (L_K/H) versus **a** channel height (H), **b** pitch ratio (p/w) and **c** liquid–solid bonding factor (β) with different shapes of roughening element. Data for the smooth (*smt*) cases are from Sun et al. (2010). The *solid line* is a guide for the eye

Fig. 15 Variation of pressure gradient ($-dp/dx$) versus **a** channel height (H), **b** pitch ratio (p/w) and **c** liquid–solid bonding factor (β) with different shapes of roughening element. Data for the smooth (*smt*) cases are from Sun et al. (2010). The *solid line* is a guide for the eye

4 Conclusions

A parametric study is carried out using a molecular dynamics–continuum hybrid simulation method to examine the effects of liquid–solid bonding strength and surface topology on the velocity and temperature boundary conditions for liquid flow in micro/nanochannels. The conclusions are as follows:

1. The velocity boundary condition shifts from significant slip to locking due to the blocking of the roughening element. The locking range and temperature jump both apparently decrease with increasing H and eventually collapse to analytical solutions (with non-slip boundary conditions). The blocking influence becomes weaker with increasing p/w and becomes more appreciable with increasing β. Distorted streamlines, small eddies and appreciable density oscillation are observed in the vicinity of the wall in the flow and density fields for small p/w and large β. On the other hand, smooth streamlines and weak oscillation are observed for large p/w and small β.

2. The results indicate that L_s/H, L_K/H and $-dp/dx$ versus H clearly follow the power laws as found in the previous work (Sun et al. 2011b). The variations of L_s/H and $-dp/dx$ versus p/w seem nearly linear while L_K/H increases with increasing p/w but the rate decreases. The data for the very strong bonding cases ($\beta > 10$) seem changing unexpectedly from others, which demands further studies.

3. The effect of the shape of roughening element on the velocity and temperature boundary conditions is much less significant compared with the other factors studied.

The present work has revealed that when the channel size is small, the flow condition (shear rate), interactive condition (liquid–solid bonding) and geometric condition (surface topology) can considerably influence the velocity and temperature boundary conditions and friction. The present work is of value for potential use of adjusting or controlling velocity, temperature and friction by surface micro-machining.

References

Allen MP, Tildesley DJ (1987) Computer simulation of liquids. Clarendon Press, Oxford

Brigo L, Natali M, Pierno M, Mammano F, Sada C, Fois G, Pozzato A, dal Zilio S, Tormen M, Mistura G (2008) Water slip and friction at a solid surface. J Phys Condens Matter 20(35):354016

Byun D, Kim J, Ko HS, Park HC (2008) Direct measurement of slip flows in superhydrophobic microchannels with transverse grooves. Phys Fluids 20(11):113601

Cao BY, Chen M, Guo ZY (2006) Liquid flow in surface-nanostructured channels studied by molecular dynamics simulation. Phys Rev E 74:066311

Curtin WA (1987) Density-functional theory of the solid–liquid interface. Phys Rev Lett 59(11):1228–1231

Delgado-Buscalioni R, Coveney PV (2003) Continuum–particle hybrid coupling for mass, momentum, and energy transfers in unsteady fluid flow. Phys Rev E 67(4):046704

Delgado-Buscalioni R, Coveney PV, Riley GD, Ford RW (2005a) Hybrid molecular–continuum fluid models: implementation within a general coupling framework. Philos Trans R Soc A 363(1833):1975–1985

Delgado-Buscalioni R, Flekkoy EG, Coveney PV (2005b) Fluctuations and continuity in particle–continuum hybrid simulations of unsteady flows based on flux-exchange. Europhys Lett 69(6):959–965

Flekkoy EG, Wagner G, Feder J (2000) Hybrid model for combined particle and continuum dynamics. Europhys Lett 52(3):271–276

Gad-el-Hak M (1999) The fluid mechanics of microdevices—the Freeman scholar lecture. J Fluids Eng Trans ASME 121(5):5–33

Hao PF, Wong C, Yao ZH, Zhu KQ (2009) Laminar drag reduction in hydrophobic microchannels. Chem Eng Technol 32(6):912–918

Hu GQ, Li DQ (2007) Multiscale phenomena in microfluidics and nanofluidics. Chem Eng Sci 62(13):3443–3454

Huisman WJ, Peters JF, Zwanenburg MJ, de Vries SA, Derry TE, Abernathy D, van der Veen JF (1997) Layering of a liquid metal in contact with a hard wall. Nature 390(6658):379–381

Kim BH, Beskok A, Cagin T (2008a) Molecular dynamics simulations of thermal resistance at the liquid-solid interface. J Chem Phys 129:174701

Kim BH, Beskok A, Cagin T (2008b) Thermal interactions in nanoscale fluid flow: molecular dynamics simulations with solid–liquid interfaces. Microfluid Nanofluid 5(4):551–559

Li Q, He G-W (2009) An atomistic-continuum hybrid simulation of fluid flows over superhydrophobic surfaces. Biomicrofluidics 3(2):22409

Liu J, Chen SY, Nie XB, Robbins MO (2007) A continuum-atomistic simulation of heat transfer in micro- and nano-flows. J Comput Phys 227:279–291

Magnussen OM, Ocko BM, Regan MJ, Penanen K, Pershan PS, Deutsch M (1995) X-ray reflectivity measurements of surface layering in liquid mercury. Phys Rev Lett 74(22):4444–4447

Maruyama S (2000) Molecular dynamics method for microscale heat transfer. In: Minkowycz WJ, Sparrow EM (eds) Advances in numerical heat transfer. Taylor and Francis, New York, vol 2, pp 189–226

Maruyama S, Kimura T (1999) A study on thermal resistance over a solid–liquid interface by the molecular dynamics method. Therm Sci Eng 7(1):63–68

Mohamed KM, Mohamad AA (2010) A review of the development of hybrid atomistic-continuum methods for dense fluids. Microfluid Nanofluid 8(3):283–302

Nagayama G, Cheng P (2004) Effects of interface wettability on microscale flow by molecular dynamics simulation. Int J Heat Mass Transf 47(3):501–513

Nie XB, Chen SY, E WN, Robbins MO (2004a) A continuum and molecular dynamics hybrid method for micro- and nano-fluid flow. J Fluid Mech 500:55–64

Nie XB, Chen SY, Robbins MO (2004b) Hybrid continuum-atomistic simulation of singular corner flow. Phys Fluids 16(10):3579–3591

Nie XB, Robbins MO, Chen SY (2006) Resolving singular forces in cavity flow: multiscale modeling from atomic to millimeter scales. Phys Rev Lett 96(13):134501

NIST (2005) Thermophysical properties of fluid systems, National Institute of Standards and Technology (NIST)

O'Connell ST, Thompson PA (1995) Molecular dynamics-continuum hybrid computations: a tool for studying complex fluid flows. Phys Rev E 52(6):R5792–R5795

Rapaport DC (2004) The art of molecular dynamics simulation. Cambridge University Press, Cambridge

Regan MJ, Kawamoto EH, Lee S, Pershan PS, Maskil N, Deutsch M, Magnussen OM, Ocko BM, Berman LE (1995) Surface layering in liquid gallium—an X-ray reflectivity study. Phys Rev Lett 75(13):2498–2501

Sikkenk JH, Indekeu JO, Vanleeuwen JMJ, Vossnack EO (1987) Molecular-dynamics simulation of wetting and drying at solid–fluid interfaces. Phys Rev Lett 59(1):98–101

Sofos FD, Karakasidis TE, Liakopoulos A (2009) Effects of wall roughness on flow in nanochannels. Phys Rev E 79(2):026305

Stoddard SD, Ford J (1973) Numerical experiment on the stochastic behavior of a Lennard-Jones gas system. Phys Rev A 8(3):1504–1512

Sun J, He YL, Tao WQ (2009) Molecular dynamics–continuum hybrid simulation for condensation of gas flow in a microchannel. Microfluid Nanofluid 7(3):407–422

Sun J, He YL, Tao WQ (2010) Scale effect on flow and thermal boundaries in micro-/nano-channel flow using molecular dynamics-continuum hybrid simulation method. Int J Numer Methods Eng 81(2):207–228

Sun J, He YL, Tao WQ (2011a) A molecular dynamics study on heat and mass transfer in condensation over smooth/rough surface. Int J Numer Methods Heat Fluid Flow 21(2):244–267

Sun J, He YL, Tao WQ, Yin X, Wang HS (2011b) Roughness effect on flow and thermal boundaries in microchannel/nanochannel flow using molecular dynamics–continuum hybrid simulation. Int J Numer Methods Eng. doi:10.1002/nme.3229

Swartz ET, Pohl RO (1989) Thermal boundary resistance. Rev Mod Phys 61(3):605–668

Thompson PA, Troian SM (1997) A general boundary condition for liquid flow at solid surfaces. Nature 389(6649):360–362

Versteeg HK, Malalasekera W (1995) An introduction to computational fluid dynamics: the finite volume method. Longman Scientific and Technical, Harlow

Voronov RS, Papavassiliou DV, Lee LL (2006) Boundary slip and wetting properties of interfaces: correlation of the contact angle with the slip length. J Chem Phys 124(20):204701

Voronov RS, Papavassiliou DV, Lee LL (2007) Slip length and contact angle over hydrophobic surfaces. Chem Phys Lett 441(4–6):273–276

Voronov RS, Papavassiliou DV, Lee LL (2008) Review of fluid slip over superhydrophobic surfaces and its dependence on the contact angle. Ind Eng Chem Res 47(8):2455–2477

Wagner G, Flekkoy E, Feder J, Jossang T (2002) Coupling molecular dynamics and continuum dynamics. Comput Phys Commun 147(1–2):670–673

Wang YC, He GW (2007) A dynamic coupling model for hybrid atomistic-continuum computations. Chem Eng Sci 62(13):3574–3579

Woolford B, Maynes D, Webb BW (2009) Liquid flow through microchannels with grooved walls under wetting and superhydrophobic conditions. Microfluid Nanofluid 7(1):121–135

Xu JL, Li YX (2007) Boundary conditions at the solid-liquid surface over the multiscale channel size from nanometer to micron. Int J Heat Mass Transf 50(13–14):2571–2581

Xue L, Keblinski P, Phillpot SR, Choi SUS, Eastman JA (2003) Two regimes of thermal resistance at a liquid–solid interface. J Chem Phys 118(1):337–339

Xue L, Keblinski P, Phillpot SR, Choi SUS, Eastman JA (2004) Effect of liquid layering at the liquid-solid interface on thermal transport. Int J Heat Mass Transf 47:4277–4284

Yen TH, Soong CY, Tzeng PY (2007) Hybrid molecular dynamics–continuum simulation for nano/mesoscale channel flows. Microfluid Nanofluid 3:665–675

Yi P, Poulikakos D, Walther J, Yadigaroglu G (2002) Molecular dynamics simulation of vaporization of an ultra-thin liquid argon layer on a surface. Int J Heat Mass Transf 45(10):2087–2100